Soft Matter

Interfacially Compatibilized PI/PDMS Blends with Reduced Octadecylamine-Functionalized Graphene Oxide: Morphological and Rheological properties

Journal:	*Soft Matter*
Manuscript ID	SM-ART-07-2021-001057.R1
Article Type:	Paper
Date Submitted by the Author:	18-Sep-2021
Complete List of Authors:	Nasrollah Gavgani, Jaber; Amirkabir University of Technology Goharpey, Fatemeh; Amirkabir University of Technology, Polymer Engineering Velankar, Sachin; University of Pittsburgh, Department of Chemical Engineering

Interfacially Compatibilized PI/PDMS Blends with Reduced Octadecylamine-Functionalized Graphene Oxide: Morphological and Rheological properties

Jaber Nasrollah Gavgani[1], Fatemeh Goharpey[1*], Sachin Velankar[2]

[1]Department of Polymer Engineering and Color Technology, Amirkabir University of Technology, P.O.Box-15875-4413, Tehran, Iran

[2]Department of Chemical Engineering, Department of Mechanical Engineering and Materials Science, University of Pittsburgh, Pittsburgh, Pennsylvania 15261

Abstract

We investigate the interfacial compatibilization effect of reduced octadecylamine-functionalized graphene oxide (ODA-GO) on the morphological and rheological properties of immiscible homopolymer blends of polydimethylsiloxane (PDMS) and polyisoprene (PI). We prepared droplet-matrix blends with a PI:PDMS ratio of 30:70 or 70:30 and interfacially localized ODA-GO stabilizer loadings from 0.1% to 1%. Blends were examined by optical microscopy and rheometry. Both blends show typical droplet-matrix morphology with stabilized round drops that do not stick together. At ODA-GO content, smaller drops were observed in PI-continuous blends as compared to the PDMS-continuous blend suggesting that the effects of particles are not symmetric in the two cases. At sufficiently high ODA-GO loadings, flow-induced coalescence is suppressed almost completely. Dynamic oscillatory rheology broadly confirm the morphological observations. Specifically, all blends show an interfacial relaxation process that is distinct from the bulk viscoelasticity, and the dependence of this process on GO content and flow conditions confirms the compatibilizing effect of the ODA-GO. This work provides a strategy for interfacially-compatibilizated polymer blends with specific properties for practical applications.

Keywords: ODA-GO, Interfacial compatibilization, Polymer blends, Morphology, Rheology

Introduction

[*]Corresponding Author; Email address: goharpey@aut.ac.ir
Tel: +982164542437

Many commercial plastic products are realized by blending together immiscible polymers. These multiphase materials are attractive as one can adjust their properties through morphological control, which, in turn, can be controlled during processing. During melt processing, the blend morphology is influenced by breakup and coalescence phenomena [1-3], which can be tuned by interfacially-active compatibilizers. A classic compatibilizer consists of the premade block copolymer or in-situ reactive compatibilizer which not only leads to a refined morphology and improved interfacial adhesion but also inhibits coalescence and improves morphology stabilization [2, 4-7]. Alternatively, it has been found that nanoparticles can act as effective compatibilizers if they are organomodified by chemical grafting [8-12] or ion exchange [13-15]. Such a modification leads to better dispersion and their excellent compatibility with the involved polymers [16, 17].

More recently, some studies reported the apparent compatibilization effect of nanoparticles in immiscible polymer blends such as Pickering emulsions, although, the compatibilization mechanisms are still unclear [18-24]. For example, some papers proposed that interfacial localization of clay nanoparticles leads to reduced interfacial tension [25, 26] even though precisely defining an interfacial tension is difficult for blends with particles at the interface. On the other hand, the compatibilization effect of clay nanoparticles was not observed for ternary blends of polyethylene/polyamide/clay nanoparticles [18, 27]. This observation can be possibly ascribed to not only the complexity of interface but also molecular characteristics of both immiscible polymer phases leading to many defects [20].

Graphene introduced a leading candidate in reinforcement, optical, electrical, and thermal conductivity. As a precursor of graphene, graphene oxide (GO) can be readily reduced with both chemical and thermal approaches [28]. However, the surface of GO must be functionalized to enhance its dispersion in hydrophobic immiscible polymers [19, 29-32]. Therefore, including oxygen-containing groups provides active sites for the chemical modification of GO, leading to interfacial localization of graphene between immiscible polymers [33-37].

The work aimed to explore droplet stabilization with reduced octadecylamine-functionalized GO (ODA-GO) as interfacial compatibilizer in immiscible polymer blends of polyisoprene (PI) and polydimethylsiloxane (PDMS). We first demonstrate an efficient approach to functionalize and

in situ reduce GO with octadecylamine (ODA). Then, we followed the interfacial compatibilization effect of ODA-GO on the morphological and rheological properties of PI/PDMS blends.

Experimental

Materials

Blends were prepared from two immiscible polymers: PI (grade LIR30) and PDMS supplied from Kuraray and Rhodia, respectively. Table 1 gives the main characteristic of the two polymers and surface tensions of the polymers which are measured by the pendant drop method at room temperature.

Table 1. Materials used.

Material	M_w (g/mole)[a]	$\eta_{25°C}$ (Pa.s)	Surface tension (mN/m)	Supplier
PI	29 000	131	19.2	Kuraray
PDMS	135 600	96	35.9	Rhodia

[a] Value quoted by the supplier.

Natural graphite flakes, octadecylamine (99%), fuming nitric acid (65–68%), concentrated sulfuric acid (95–98%), concentrated hydrochloric acid (36–38%), potassium permanganate (98%), hydrogen peroxide, fluorescein isothiocyanate (FITC), tetrahydrofuran (THF, 99.7%) methanol (99.5%), ethanol (99.7%) were all analytically pure and purchased from Sigma Aldrich Co (Germany).

Functionalization of GO with ODA

GO was synthesized from expanded graphite using the modified chemical method (see supporting information) [38]. In a typical procedure for preparing ODA-GO, 300 mg GO was dispersed in 200 ml deionized water via water bath sonication. Subsequently, ODA (300 mg) in 80 ml ethanol solution was added. The mixture was refluxed with mechanical stirring at 100 °C for 48 h and filtered through a polyamide membrane with an average pore size of 0.45 µm. The filtered material was thoroughly washed with THF 4 times to remove any unreacted, free ODA. Finally, the filtrate cake was dried in an oven at 80 °C for 24 h. For fluorescent images, FITC was loaded on ODA-GO by sonicating FITC solution (0.05 $mg.mL^{-1}$, 2 mL) with a suspension of ODA-

GO in THF (2 mg.mL^{-1}, 1 mL) for 30 min to mix them, followed by stirring overnight. In this case, the isocyanate groups of FITC were reacted with GO-ODA hydroxyl groups at room temperature. This reaction resulted in fluorescently tagged ODA-GO. Free FITC was removed by rinsing and centrifugation.

Preparation of PI/PDMS/ODA-GO blends

PI and PDMS were first blended in either a 30:70 or 70:30 weight ratio. Then, the as-prepared ODA-GO was dispersed and exfoliated in PI/PDMS by batch sonication at 30 °C with the total ODA-GO loading varying between 0.1-1 wt%. Samples are named by Sx-w_{comp}, where x is the weight fraction of the PDMS phase and w_{comp} is the overall wt % of ODA-GO. For example, a 1 g sample of S30-1.0 contains 0.297 g PDMS, 0.693 g PI, and 0.01 g of ODA-GO.

Characterization

X-ray diffraction (XRD) spectra measurements were carried out using a Rigaku D/Max 2500 diffractometer with CuKα radiation (λ = 1.54 Å) at a generator voltage of 40 kV. Fourier-transform infrared spectroscopy (FTIR) was performed using an Equinox 25 Bruker (Canada). Raman spectra were measured with a Renishaw in Via Raman microscope (Britain) using a 514.5 nm He-Ne laser. X-ray photoelectron spectroscopy (XPS) data were recorded by ThermoVG RSCAKAB 250X. Elemental analysis was measured using a Flash EA1112 (Thermo Electron SPA). The contact angle was measured by Sessile Drop Technique. GO and ODA-GO films were obtained by vacuum filtration with PP membranes (an average pore size of 0.2 μm), and subsequently, dried at 80 °C for 24 h. The volume conductivities of the sample films were measured with a four-probe resistivity meter (TRS-6). Scanning electron microscope (SEM) images were analyzed by a Hitachi S4700 at an accelerating voltage of 20 kV. Transmission electron microscope (TEM) observations were performed on a Zeiss-EM10C electron microscope operating at an accelerating voltage of 80 kV. Atomic force microscopy (AFM) measurements were carried out with a Multimode SPM (Digital Instruments. Optical microscopy (OM) was performed using a Zeiss microscope (Carl Zeiss Jena 033370) at room temperature. Fluorescent images were taken using a Zeiss CLSM 700 confocal laser scanning microscope.

Rheological experiments were performed using a UDS200 rheometer (Paar Physica) equipped with a 50 mm diameter/1° cone and plate geometry, and the sample temperature of 25°C was maintained using a Peltier cell. Strain-sweep measurements were conducted at a frequency of 1 rad/s for strains ranging from 0.1% to 100%. Small amplitude oscillatory shear tests were also performed using strain amplitude of 5% and angular frequency of 0.01-1000 rad/s within the linear viscoelastic regime. After the initial small-amplitude oscillatory shear measurements, the blends were subjected to the flow protocol shown in Fig. 1. The blends were sheared at 400 Pa for 2000 strain units, and then the subsequent recovery upon cessation of shear was monitored, followed by a frequency sweep measurement (ranging from 0.01 to 1000 rad/s) at 5% strain. This sequence (shear for 2000 strain units, recovery, and frequency sweep) was repeated at successively lower stresses of 200, 100, and 50 Pa while keeping the strain equal to 2000.

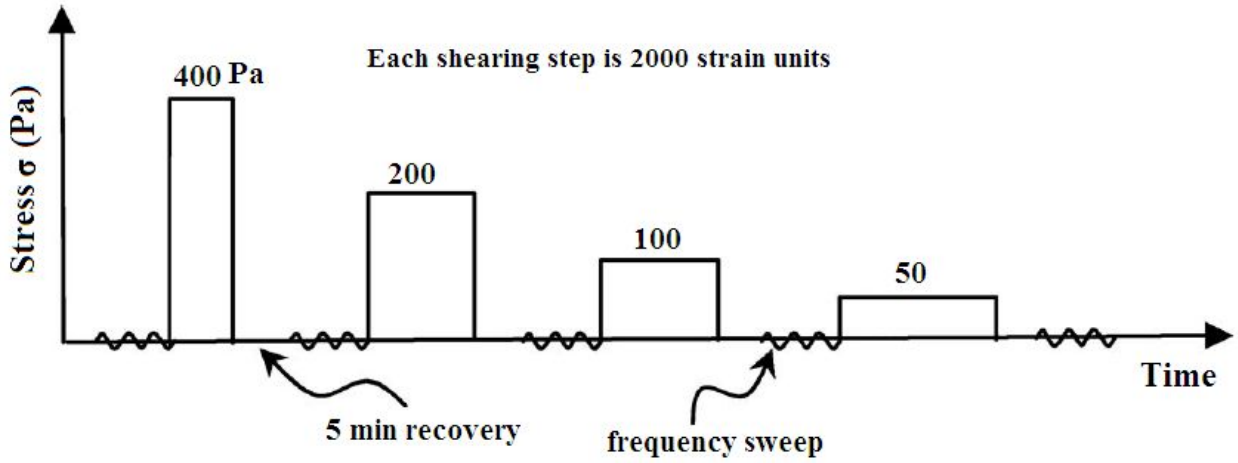

Fig. 1 Shear history for the rheology experiment.

Results and discussion

Characterization of GO and ODA-GO

GO can be dispersed well in water due to the hydroxyl, carboxyl, and epoxide groups on its surface. The average thickness of GO measured by AFM is about 0.89 nm which confirmed monolayer exfoliation (Fig. S1). The functionalization and reduction of GO with ODA by the reaction between amine groups of ODA and epoxide groups of GO through an amidation

reaction are shown in Fig. S2A. A first indication of the reduction of GO is the color change of GO aqueous solution from yellow to black after ODA addition (Fig. S2C).

Figure 2 shows the XRD patterns of GO and functionalized ODA-GO. The characteristic diffraction peak of GO is at 10.6° corresponding to an interlayer spacing of 0.86 nm which is larger than that of pristine graphite (∼ 0.34 nm) owning to substituted functional groups on carbon sheets [39]. In comparison to GO, ODA-GO presents a diffraction peak at a smaller diffraction angle. This peak is not entirely resolved by our instrument, but the peak location is almost ∼ 2.8° (d_{001} = 3.24 nm) suggesting a significant enlargement in interlayer spacing [39], which is attributed to the chemical grafting of ODA onto GO via nucleophilic substituted amidation reaction [29, 40]. The following equation can be used to predict the theoretical value of interlayer spacing: $d_{001}= T_{GO}+ T_c$, where T_{GO} is the thickness of the GO layer and T_c is the length of the rigid ODA chain [41]. The theoretically predicted length of the ODA chain was calculated based on the as-below equation (See Fig. S2B):

$$L = 2 \times \left(0.1479 \times \cos\left(\frac{180 - 110.9}{2}\right)\right) + 18 \times \left(0.1540 \times \cos\left(\frac{180 - 109.5}{2}\right)\right) = 2.5074\ nm \quad (1)$$

If the average thickness of the GO layer of 0.89 nm is used, d_{001} is calculated to be 3.3nm, which is in agreement with the estimated experimental value (3.24 nm). In addition, a broad peak at ∼24.7° appears, which may be due to the restacking of the exfoliated and modified graphene sheets [30, 42].

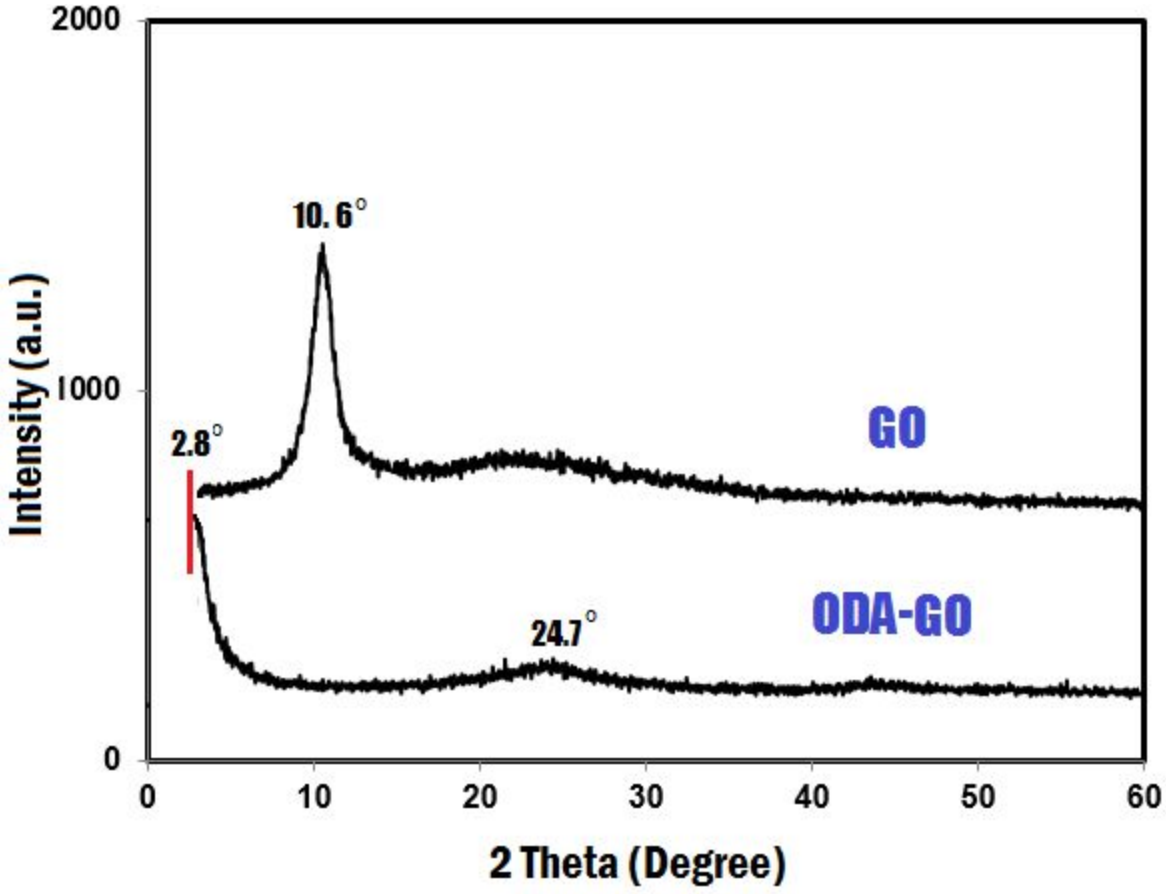

Fig. 2 XRD pattern of GO and ODA-GO.

As reported in [40], the nucleophilic substituted amidation reaction between the primary amine groups of ODA with the epoxide groups of GO occurred during the refluxing. Figure 3 shows the FTIR spectra of GO, ODA, and ODA-GO. The typical peaks of GO appear at 1710 cm^{-1} (C=O carboxyl stretching vibration), 1642 cm^{-1} (C=C in an aromatic ring), 1385 cm^{-1} (C–OH stretching), and 1030–1160 cm^{-1} (C–O–C in epoxide). In addition, the wide peak appearing at 3000-3500 cm^{-1} could be assigned to the hydroxyl groups. While in the FTIR spectrum of ODA-GO, two new peaks at 2919 cm^{-1} and 2848 cm^{-1} resulting from the $–CH_2$ stretching of the octadecyl chain together with the peak at 720 cm^{-1} imply the existence of the octadecyl chain on ODA-GO (Fig. S2). Furthermore, a new peak at 1178 cm^{-1} (C–N stretching vibration) appeared, indicating the formation of C–NH–C bands due to the chemical grafting of ODA to GO surface via nucleophilic substituted amidation reaction between the amine group of ODA and the epoxide group of GO. This conclusion is also supported by the presence of new peaks of deformation and stretching

of N–H in –C–NH_2 groups at 733 and 1563 cm^{-1}, and the peak of H-bond interaction between –NH_2 and oxygen-containing groups of GO at 3219 cm^{-1}. This reaction is also supported by the disappearance of the peaks of the primary amine group at 3332 cm^{-1} and 3264 cm^{-1}. All these results confirm the intercalation and chemical reaction of ODA with GO.

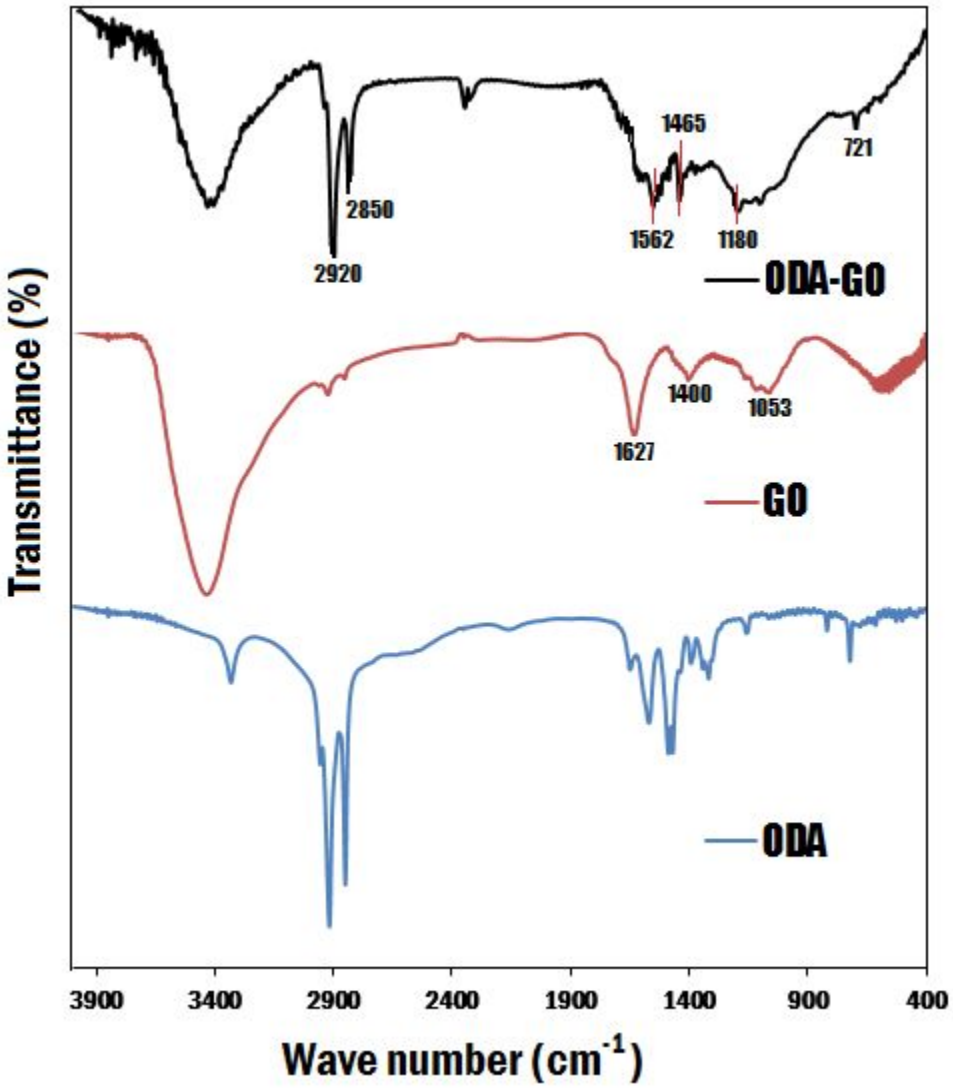

Fig. 3 FTIR spectra of ODA, GO, and ODA-GO.

XPS was employed to evaluate the chemical bonds formed on the surface of GO before and after its functionalization with ODA (Fig. 4). Typically, the C 1s peak region of GO can be fitted into four curves. The binding energies at 285.0 eV, 286.7 eV, 287.2 eV, and 289.4 eV are assigned to unoxidized graphite carbon skeleton (C–C), hydroxyl group (C–OH), epoxide group

(–C–O–C–), and carboxyl group (–O–C=O), respectively. However, in the XPS spectrum of ODA-GO, the peaks of the oxygen-containing groups are greatly weakened in intensity, i.e. the atomic ratio of carbon and oxygen (C/O) increased from 2.6 to 7.8, and a new peak at 285.4 eV corresponding to C–N appears, demonstrating the grafting of GO with ODA.

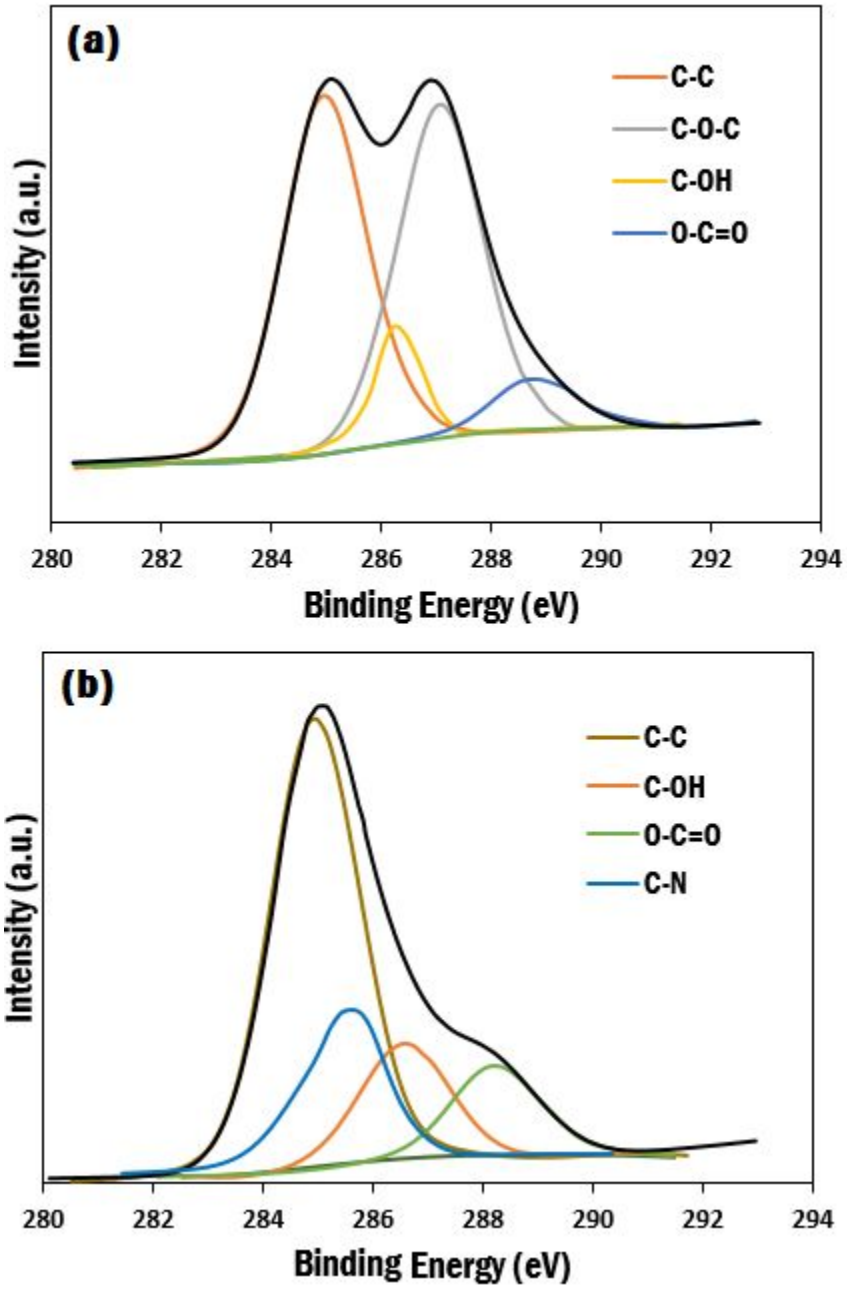

Fig. 4 C 1s XPS spectra of (a) GO and (b) ODA-GO.

The reduction of GO was also reflected in the enhanced thermal stability of GO–ODA (Fig. 5). As a small molecule, ODA exhibits low thermal stability and was almost fully degraded when the temperature was increased to 250 °C; while GO mainly decomposed from 170 °C to 270 °C owing to the decomposition of the oxygen functional groups, yielding CO_2, CO and vapor. However, ODA-GO shows a mass loss of about 10 wt% in the temperature range 160 °C to 210 °C, which is attributed to the physically adsorbed ODA. At higher temperatures, the mass loss of GO–ODA may be attributed to the chemically bonded ODA and GO itself. The mass losses of GO and ODA-GO at 580 °C are 38.4 wt% and 55.9 wt%, respectively. As the content of ODA in ODA-GO measured by elemental analysis is 37 wt%, while based on mass loss of ODA-GO, the content of covalently grafted ODA is 44.1 wt%.

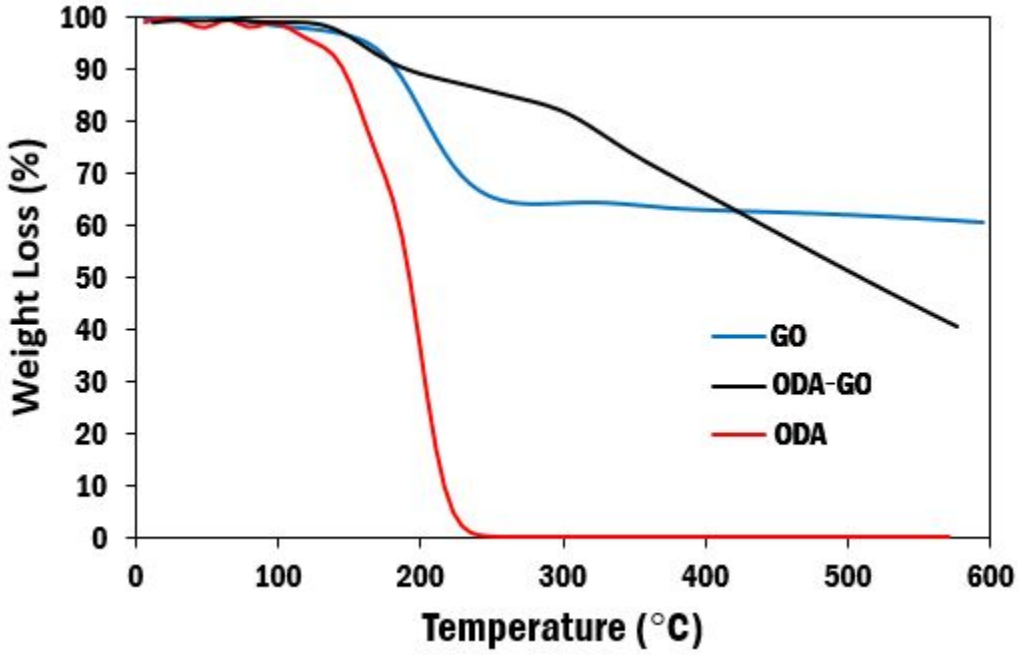

Fig. 5 TGA curves of ODA, GO, and ODA-GO.

Figure 6 shows the Raman spectra of GO and ODA-GO. It is well-recognized that the D band results from a breathing mode of j-point photons of A1g symmetry, while the G band is due to the first-order scattering of the E2g phonon of sp^2 C atoms [43]. The D band of GO is located at 1344 cm^{-1}, which results from the decrease in the size of the in-plane sp^2 domains due to the extensive oxidation. The G band of GO becomes at 1596 cm^{-1} owing to the presence of isolated double bonds. After the refluxing of GO with ODA, however, a marginal increase in the D to G

band intensity ratio, I_D/I_G, from 1.05 to 1.08, as well as a marginal redshift of the G peak position from 1596 cm^{-1} to 1585 cm^{-1} upon reduction to ODA-GO, thus indicating the restoration of the graphitic sp^2 network. The decrease in the size of the newly formed graphene-like sp^2 domains may also be partly responsible for the increase in the intensity ratio, I_D/I_G for ODA-GO [43].

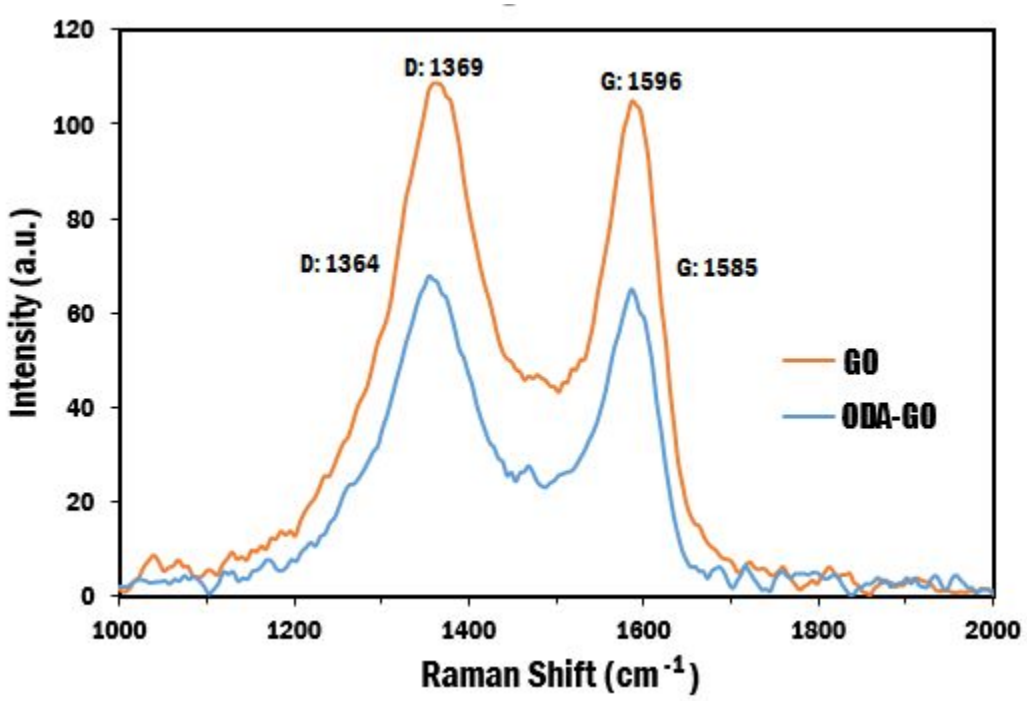

Fig. 6 Raman spectra of GO and ODA-GO.

Figure 7a presents a typical OM image of the GO sheets synthesized in this study, confirming a lateral size of tens of micrometers. The corresponding SEM micrograph, Fig. 7b, complements the OM image. The GO sheets, shown in black, had a lateral size predominantly on the order of 10–25 µm. However, small ODA-GO sheets, typically 5–10 µm in diameter were also observed, which are thought to be inevitable due to breakages during the exfoliation process (Fig. 7c). The TEM image, Fig. 7c, indicates that the ODA-GO sheets indeed consisted of single layers whose size was more than several micrometers, in good agreement with the OM observations.

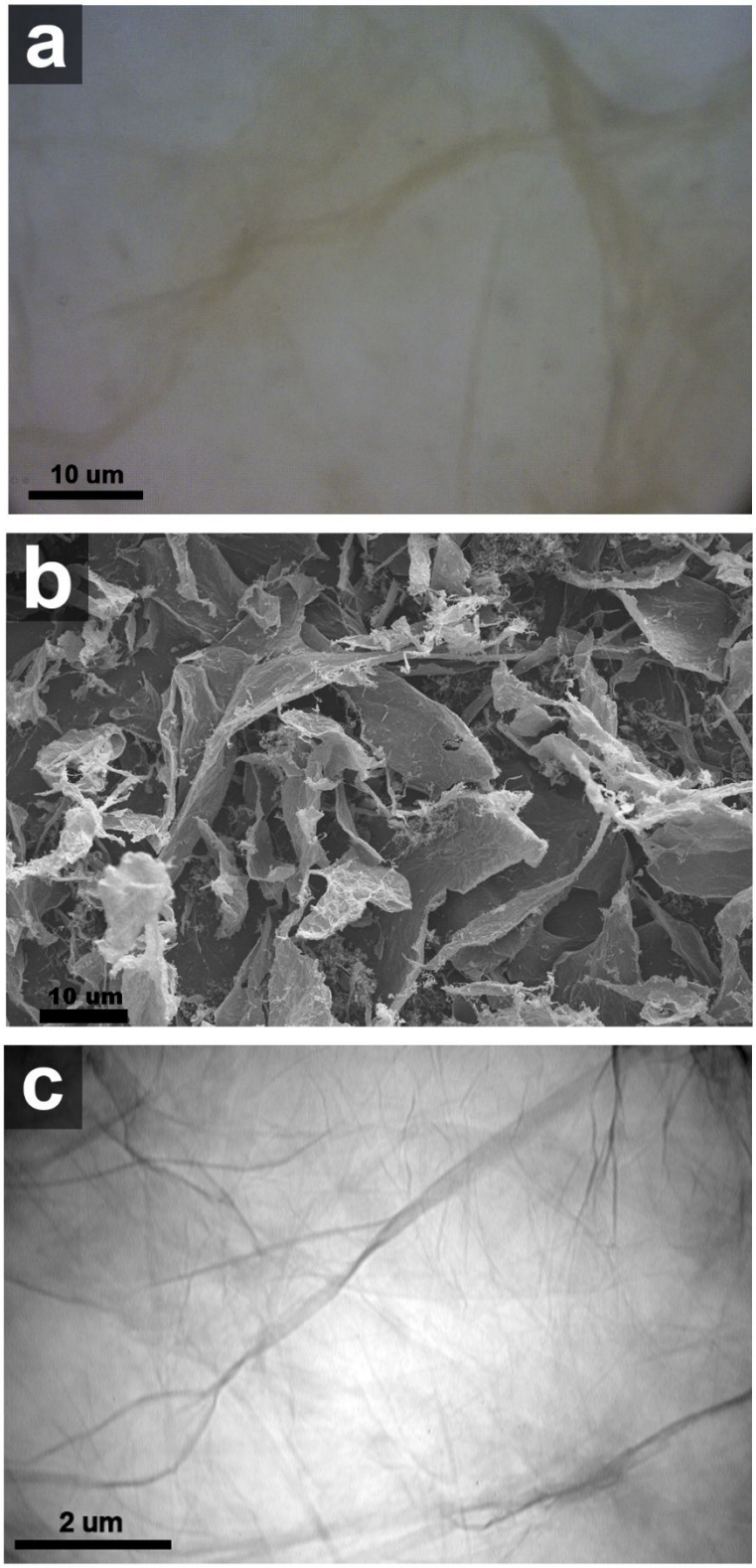

Fig. 7 (a) OM, (b) SEM images of GO (c) TEM image of ODA-GO.

GO is completely dispersed in H_2O due to polar features (brown solution, left vial, Fig. S2C), while the ODA-GO is dispersed in THF owing to the hydrophobic effect of grafting octadecyl chain on the GO surface (black solution, right vial, Fig. S2C). Moreover, it is believed to be due to the presence of a rigid long octadecyl chain of ODA that acts as covalently linked nanoscale spacers impeding the face-to-face stacking of GO sheets [29]. Therefore, owing to the chemical reduction with ODA, ODA-GO film as shown in Fig. 8, is electrically conductive with an electrical conductivity of 11 S/m, which is much higher than that of GO film (6×10^{-4} S/m).

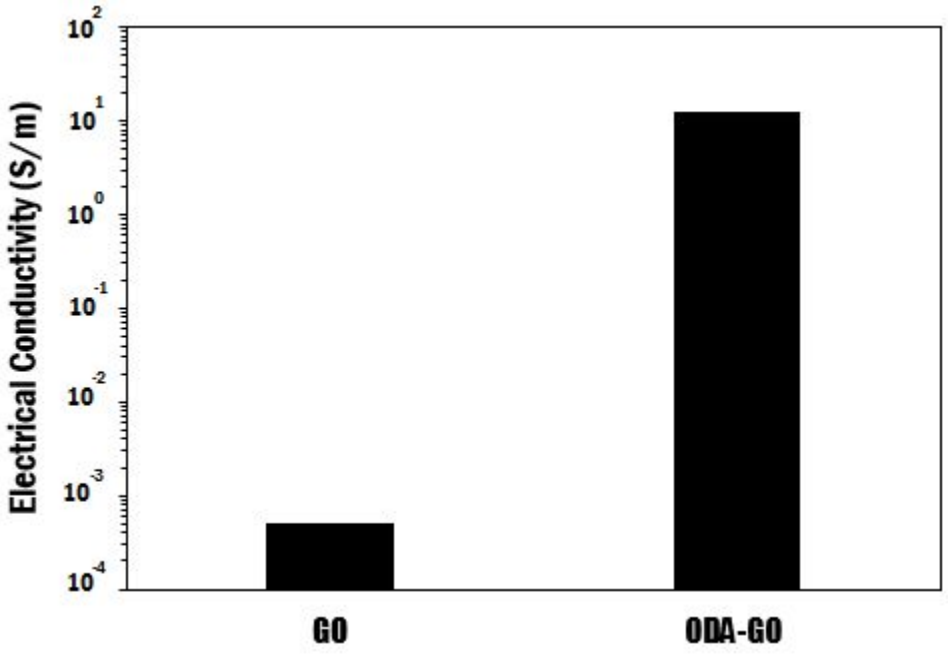

Fig. 8 Electrical conductivity of GO and ODA-GO films.

Effect of ODA-GO content on PI/PDMS blend morphology

Before evaluating the PI/PDMS blend morphology, we found that regardless of the presence or absence of ODA-GO, the minority species would always become the dispersed phase. Moreover, the phase inversion composition for PI/PDMS corresponds to a 50/50 blend. Figure 9 presents OM images of uncompatibilized S30-0 and S70-0 immediately after mixing (t=0) and under quiescent conditions at room temperature. After mixing, the drops of both blends are spherical with a large particle size (~ 20 μm). After 24 h, the drops begin to coalesce and increase in their size (~ 40 μm), suggesting rapid coalescence of the dispersed phase.

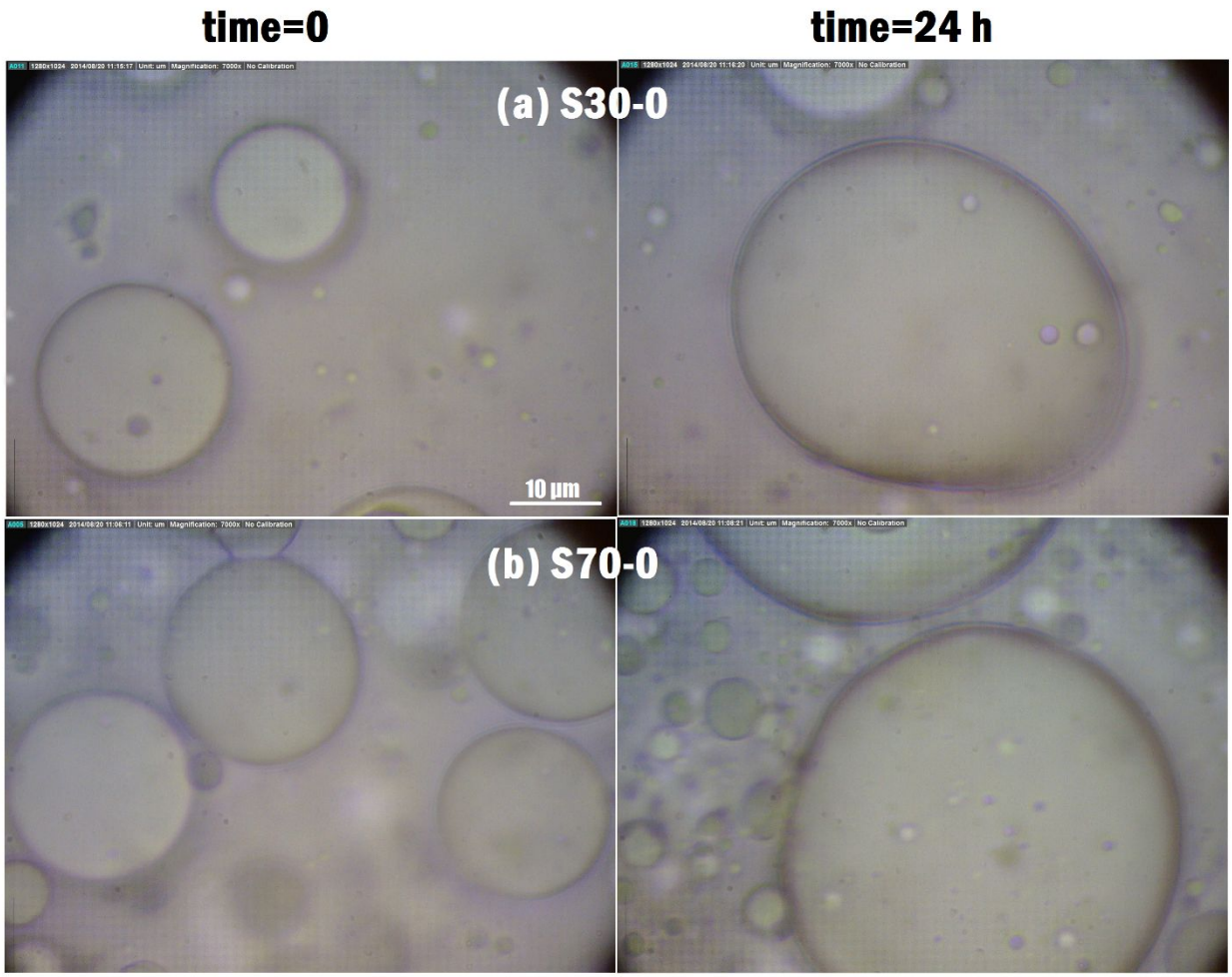

Fig. 9 Morphology of uncompatibilized blends immediately after mixing (t=0) and after 24 h under quiescent conditions at room temperature: (a) S30-0, and (b) S70-0. The scale bar of 10 microns in the top left image applies to all images.

Figure 10 presents the compatibilization effect of various ODA-GO content on S30 blends. Upon addition 0.1 wt% ODA-GO to S30 (Fig. 10a), the size of drop decreases slightly as compared to uncomaptibilized S30-0. Upon increasing the ODA-GO content in S30, the drop size decreased further to ~ 8 µm at 0.5 wt% GO and ~ 1 µm at 1 wt%GO. In all cases, the images suggest that the drop size is stable with time, suggesting complete inhibition of coalescence. Later in this paper, we will show that these effects are consistent with the interfacial localization of ODA-GO which forms a strong interfacial skin covering the drops.

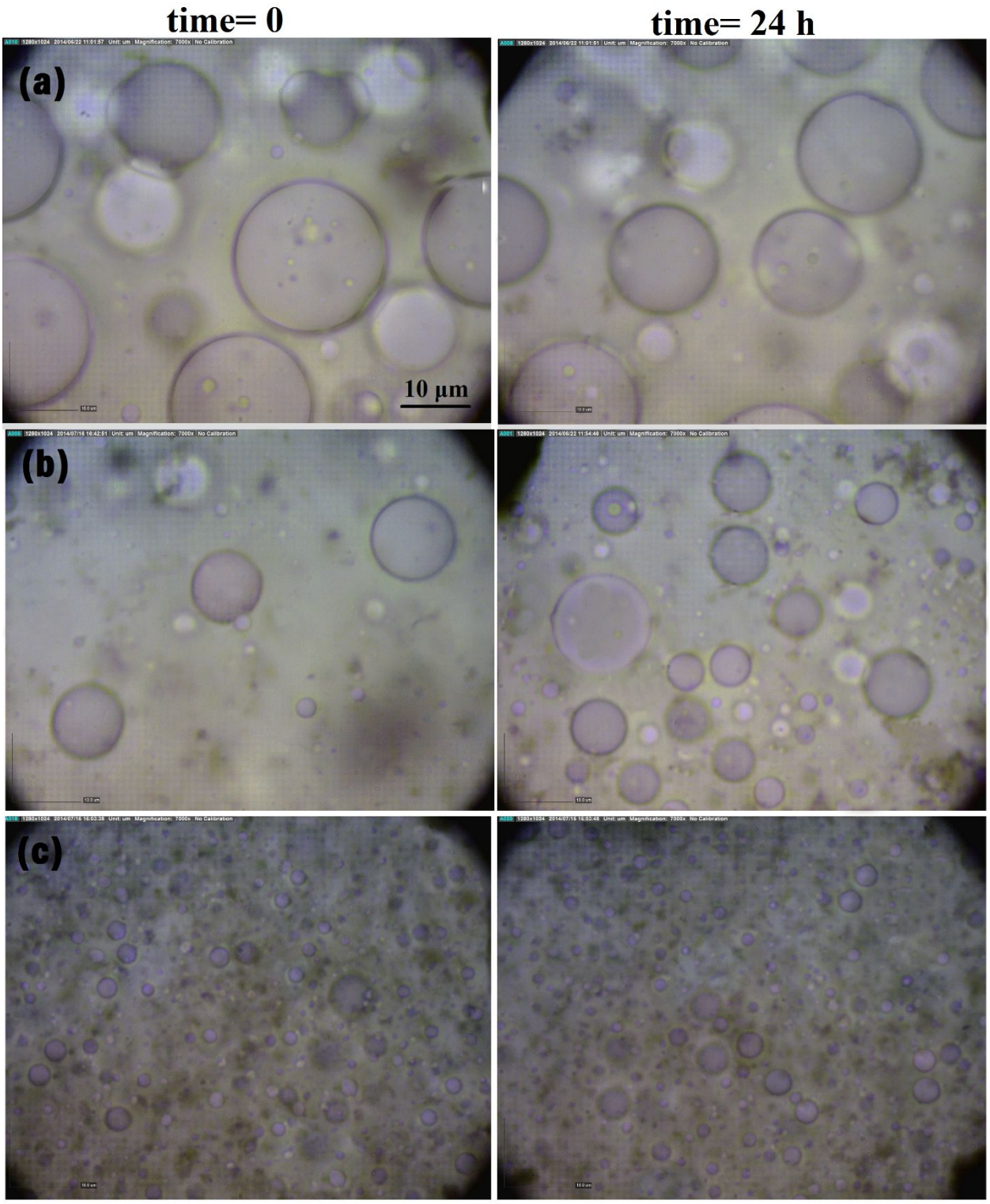
time= 0
time= 24 h
(a)
10 µm
(b)
(c)

Fig. 10 Morphology of compatibilized S30 blends with various ODA-GO content immediately after mixing (t=0) and after 24 h under quiescent conditions at room temperature: (a) S30-0.1, (b) S30-0.5, (c) S30-1. The scale bar of 10 microns in the top left image applies to all images.

The microstructures of S70 in presence of ODA-GO different content are presented in Fig. 11(a-c). Upon mixing and after 24 h of quiescent conditions, a typical droplet-matrix morphology is evident in three blends. All drops appear spherical, and clustering is not evident. However, as compared to the S30-0.5 blend, the addition of 0.5 wt% ODA-GO does not further decrease the drop size of S70-0.5. Moreover, in the presence of 1 wt% ODA-GO, although the stabilized fine PDMS drops are observed, the mean droplet size (~ 4 μm) is larger than that of S30-1. In comparison to S30-1, the drops of S70-1 is slightly larger than S30-1 droplets.

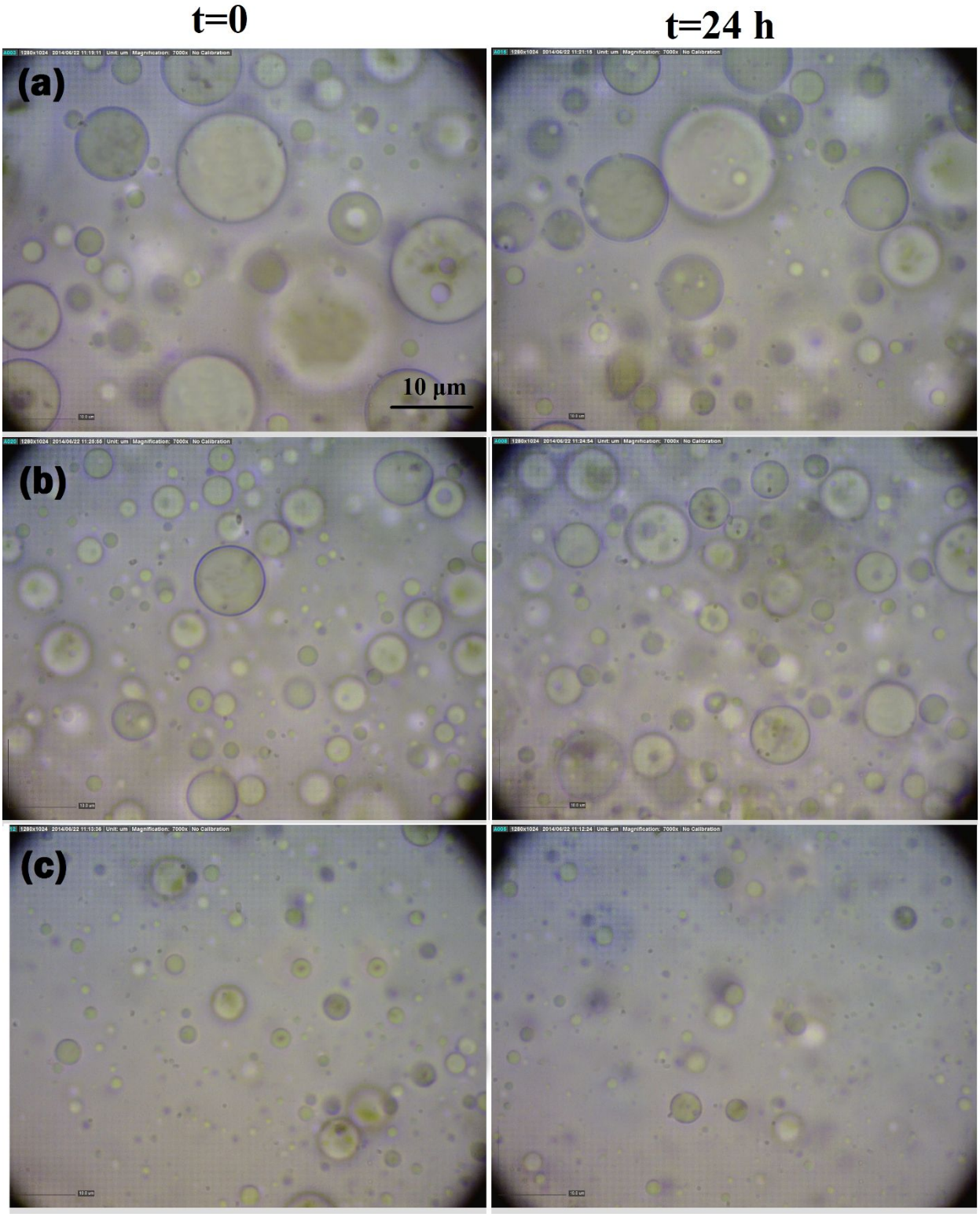
t=0
t=24 h
(a)
10 µm
(b)
(c)

Fig. 11 Morphology of compatibilized S70 blends with different ODA-GO content immediately after mixing (t=0) and after 24 h under quiescent conditions at room temperature: (a) S70-0.1, and (b) S70-0.5, (c) S70-1. The scale bar of 10 microns applies to all images.

The S30-0.5 and S70-0.5 blends were examined by fluorescence microscopy in Fig. 12(a-b), respectively. Upon the addition of a small amount of ODA-GO in both blends, the drops appear as bright green shells, suggesting that the ODA-GO adsorbed at the PI/PDMS interface. Moreover, despite the ODA-GO adsorption, the droplets appear spherical and do not appear to stick together into a network structure. In addition, despite the same imaging conditions for both samples, the green shell thickness in S30-0.5 is slightly more than in S70-0.5, suggesting that the PDMS droplets absorb more ODA-GO on their surface than PI ones. This issue is discussed in a further section.

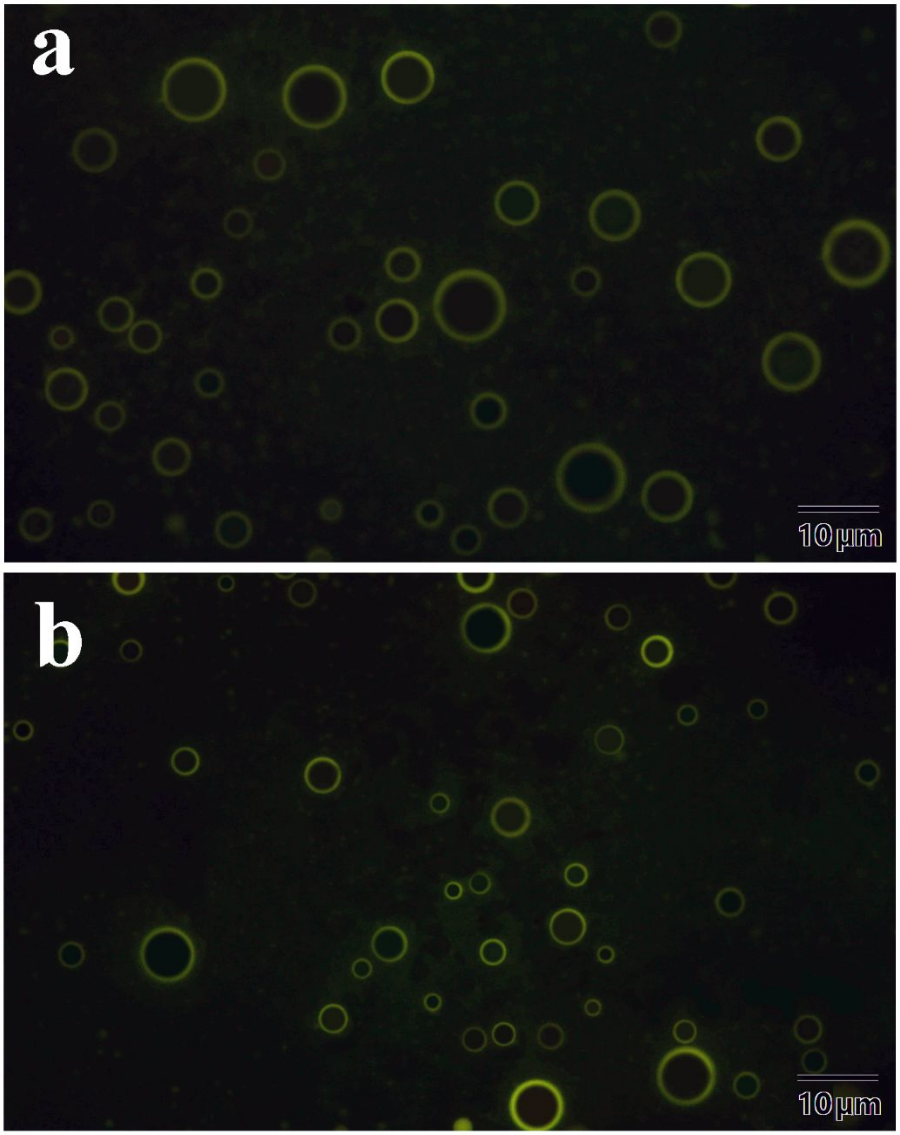

Fig. 12 The fluorescent image of (a) S30-0.5 and (b) S70-0.5.

Interfacial localization of ODA-GO in PI/PDMS blends

The interfacial localization of ODA-GO in the PDMS/PI blends can be qualitatively predicted by calculating the wetting coefficients of ODA-GO. Relevant to the current study, the wetting coefficient (ω) of ODA-GO in the PDMS/PI interface is defined as [27]

$$\omega = \cos\theta = \frac{\gamma_{ODA-GO/PDMS} - \gamma_{ODA-GO/PI}}{\gamma_{PDMS/PI}} \quad (2)$$

where θ is the three-phase contact angle of ODA-GO at the interface, and $\gamma_{ODA-GO/PDMS}$, $\gamma_{ODA-GO/PI}$, and $\gamma_{PDMS/PI}$ are the interfacial energies (or interfacial tensions) between ODA-GO and PDMS, ODA-GO and PI, and PDMS and PI, respectively. Because of the difficulties in experimentally measuring the interfacial energy between ODA-GO and polymers, all of these interfacial energies were theoretically derived, according to the Owens-Wendt's equation, using the harmonic mean of dispersive and polar part of surface energies [44, 45]. For example, $\gamma_{PDMS/PI}$ can be calculated as

$$\gamma_{PDMS/PI} = \gamma_{PDMS} + \gamma_{PI} - 2\sqrt{\gamma_{PDMS}\gamma_{PI}} = \gamma_{PDMS} + \gamma_{PI} - 2\sqrt{\gamma^d_{PDMS}\gamma^d_{PI}} - 2\sqrt{\gamma^p_{PDMS}\gamma^p_{PI}} \quad (3)$$

where γ^d and γ^p are the dispersive component and the polar component of the surface energy of the components at room temperature, respectively. Based on surface tensions of the PDMS and PI (Table 1) and eq 3, the interfacial tension between PI and PDMS ($\gamma_{PDMS/PI}$) was calculated 2.6 mN/m. On the other hand, the measured interfacial tension between PI and PDMS by the pendant drop method is found to be 2.73 mN/m. In addition, the surface tension of ODA-GO was measured based on Young and Owens-Wendt's equations. Based on Young's equation, the contact angle can be given as follows:

$$\gamma_s = \gamma_{sl} + \gamma_l \cos\theta \quad (4)$$

where γ_s, γ_l, and γ_{sl} represent the solid surface free energy, liquid surface free energy, and solid-liquid interfacial energy, respectively. θ is the contact angle between the solid surface and the liquid. The γ_{sl} was placed based on equation Owens-Wendt (eq 3):

$$(\gamma_s\gamma_l)^{0.5} = 0.5\,\gamma_l(1+\cos\theta) \quad (5)$$

$$\gamma^p + \gamma^d = \gamma \quad (6)$$

$$\left(\gamma^d_s\gamma^d_l\right)^{0.5} + \left(\gamma^p_s\gamma^p_l\right)^{0.5} = 0.5\,\gamma_l(1+\cos\theta) \quad (7)$$

According to Fig. 13, the contact angle between ODA-GO and H_2O and THF is provided in Table 2. The surface tension of H_2O and THF was presented also in Table 2 at 20 °C.

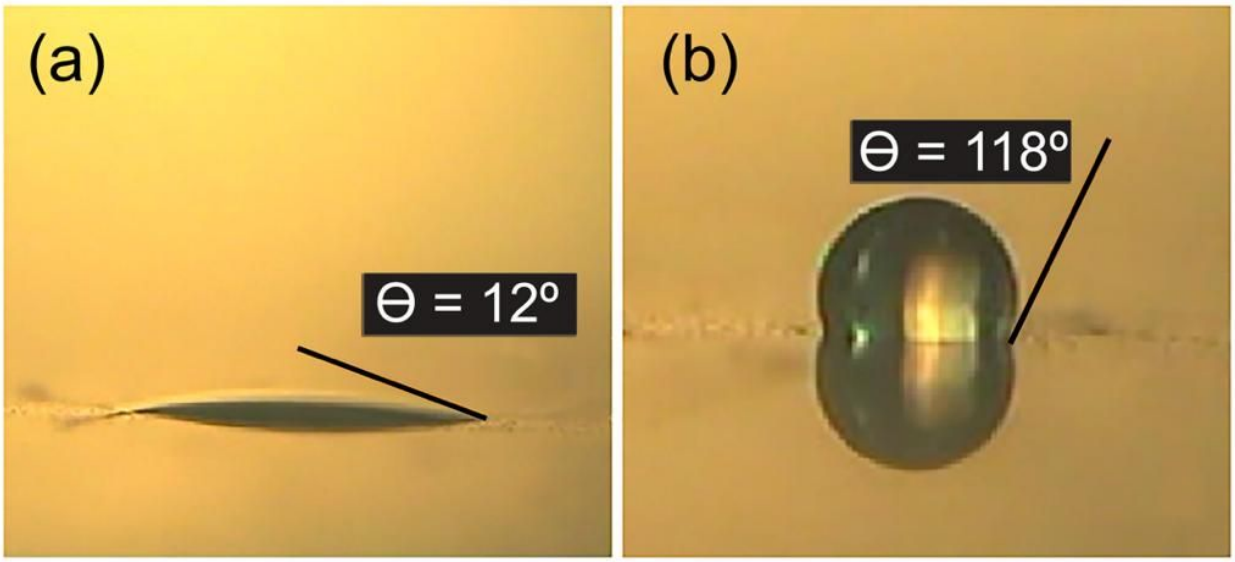

Fig. 13 Contact angle of THF (a) and H_2O (b) droplets for coated ODA-GO film.

Table 2. Average Contact Angle Measured by the Droplet on the ODA-GO Film Surface and γ^d and γ^p and γ of the H_2O and THF at 20 °C.

Materials	Contact angle	γ^d (mN/m)	γ^P (mN/m)	γ (mN/m)
H_2O	118 (2.1)	21.8	51	72.8
THF	12 (3.4)	27.4	0	27.4

[a]The numbers in parentheses show the standard deviation.

Regarding eq 7 and the result of Table 2, the γ^d and γ^p and γ of the ODA-GO were calculated to be 26.7, 0.57, and 27.27 mN/m, respectively. Therefore, using eq 3, the $\gamma_{ODA-GO/PDMS}$ and $\gamma_{ODA-GO/PI}$ are found to be 0.71 mN/m and 0.593 mN/m, respectively.

The ODA-GO thermodynamically prefers to locate at the interface between PDMS and PI when -1 < ω < 1. When ω < -1, GO-ODA locates in the PDMS phase, whereas GO-ODA remains in the PI phase when ω > 1. From the values of $\gamma_{ODA-GO/PDMS}$ and $\gamma_{ODA-GO/PI}$ and $\gamma_{PDMS/PI}$, the calculated wetting coefficient is 0.045, which suggests that ODA-GOs would be located in PDMS/PI interface. Moreover, to confirm interfacial localization of ODA-GO, we calculate the

energy required to remove one sheet of ODA-GO from a planar interface to polymer matrix PDMS can be expressed as

$$\Delta E_{int./PDMS} = A_{ODA-GO}(\gamma_{ODA-GO/PDMS} - \gamma_{ODA-GO/PI} + \gamma_{PDMS/PI}) \quad (8)$$

where $\gamma_{x/y}$is the interfacial tension between component x and y at 25 °C, and A_{ODA-GO} is the average area of a single ODA-GO sheet. Equation 8 has also been used to explain the interfacial localization of colloidal particles in water/oil Pickering- Ramsden emulsions [46, 47]. Based on eq 3, the values of $\gamma_{ODA-GO/PDMS}$, $\gamma_{ODA-GO/PI}$, and $\gamma_{PDMS/PI}$ are found to be 0.71 mN/m, 0.59 mN/m, and 2.6 mN/m, respectively and $A_{ODA-GO} = 0.03\ \mu m^2$. Hence the $\Delta E_{int./PDMS}/k_BT =$ 19812 >>1, and $\Delta E_{int./PI}/k_BT =$ 18106 >>1, where k_B is the Boltzmann constant and T is 25 °C. Since both ΔE values far exceed 1, interfacial localization of ODA-GO is strongly favorable.

Dynamic oscillatory properties of PI/PDMS blends

All blends showed linear viscoelastic behavior under strain-sweep measurements. The oscillatory frequency sweeps of PI and PDMS containing 1 wt% ODA-GO (the maximum percentage used in this study) are presented in Fig. S3, which indicate that the effect of ODA-GO on the bulk rheological behavior can be neglected in the studied range of concentrations. Therefore, any rheological changes observed in the as-prepared blends can be regarded as an interfacial effect of ODA-GO in the PI/PDMS interface.

Figure 14 shows the oscillatory frequency sweeps of the as-prepared blends S30-0.1, S30-0.5, S30-1, i.e., the blends were tested immediately after degassing with no preshearing other than that experienced during sample loading. As can be seen that G' and |η*| show a pronounced shoulder at lower frequencies that have been attributed to interfacial relaxation processes, chiefly, relaxation of the drop shape. With increasing ODA-GO loading, the following changes occur: The shoulder in G' moves to lower frequencies, and |η*| shows an increasing trend with decreasing frequency. Moreover, the shoulder in G' becomes less prominent, the slope of log(G') vs log(frequency) deviates from a slope of 2 at low frequencies, and |η*| shows an increasing trend with decreasing frequency.

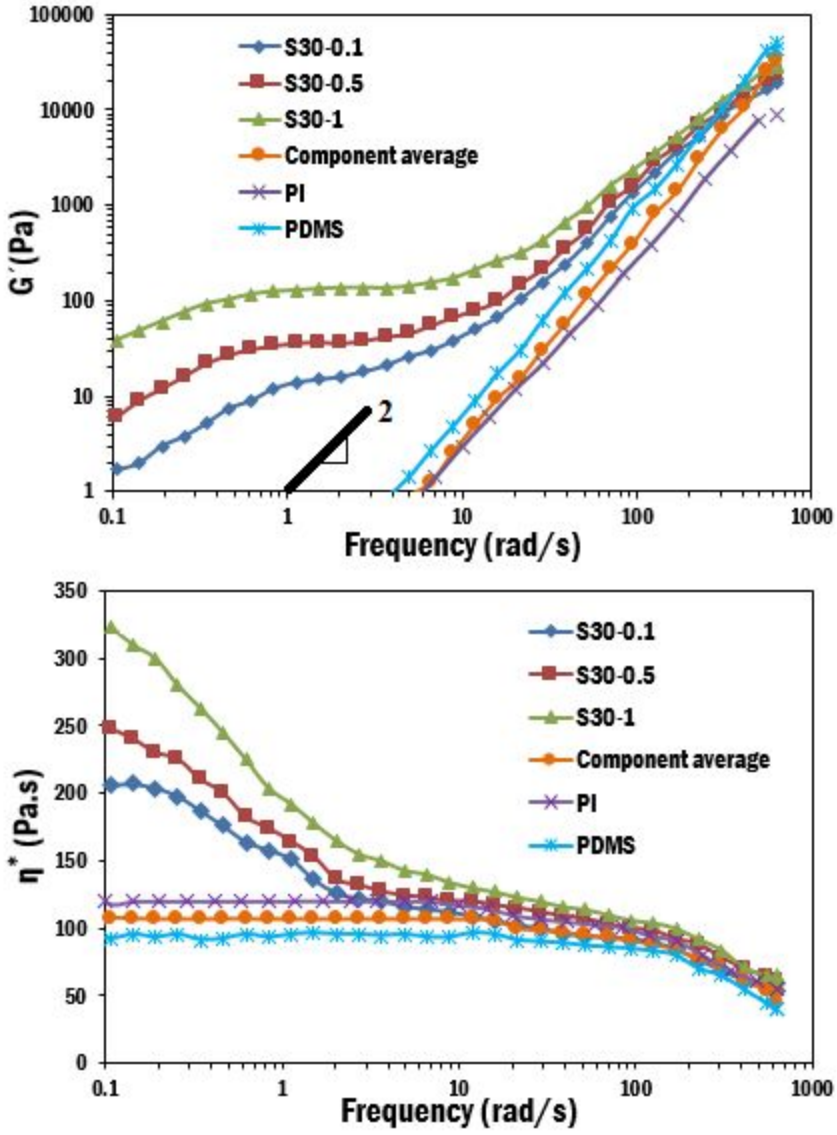

Fig. 14 As loaded oscillatory for varying ODA-GO contents in PI-continuous blends.

The as-loaded oscillatory properties for the S70-1 are presented in Fig. 15, along with S70-0.5 and S70-0.1. At low ODA-GO loadings, the results resemble those of Fig. 14, and the interfacial relaxation process is clearly evident. The chief difference is that the deviation from liquid-like behavior is less prominent in S70-1 as compared to S30-1. In addition, the S70-1 has a smaller complex viscosity than S30-1. These results show that the interfacially-adsorped particles induce strong interfacial viscoelasticity when PI is the continuous phase, and produce smaller

drops as compared to PDMS-continuous blends. Thus the effect of particles is asymmetric, depending on which phase is continuous.

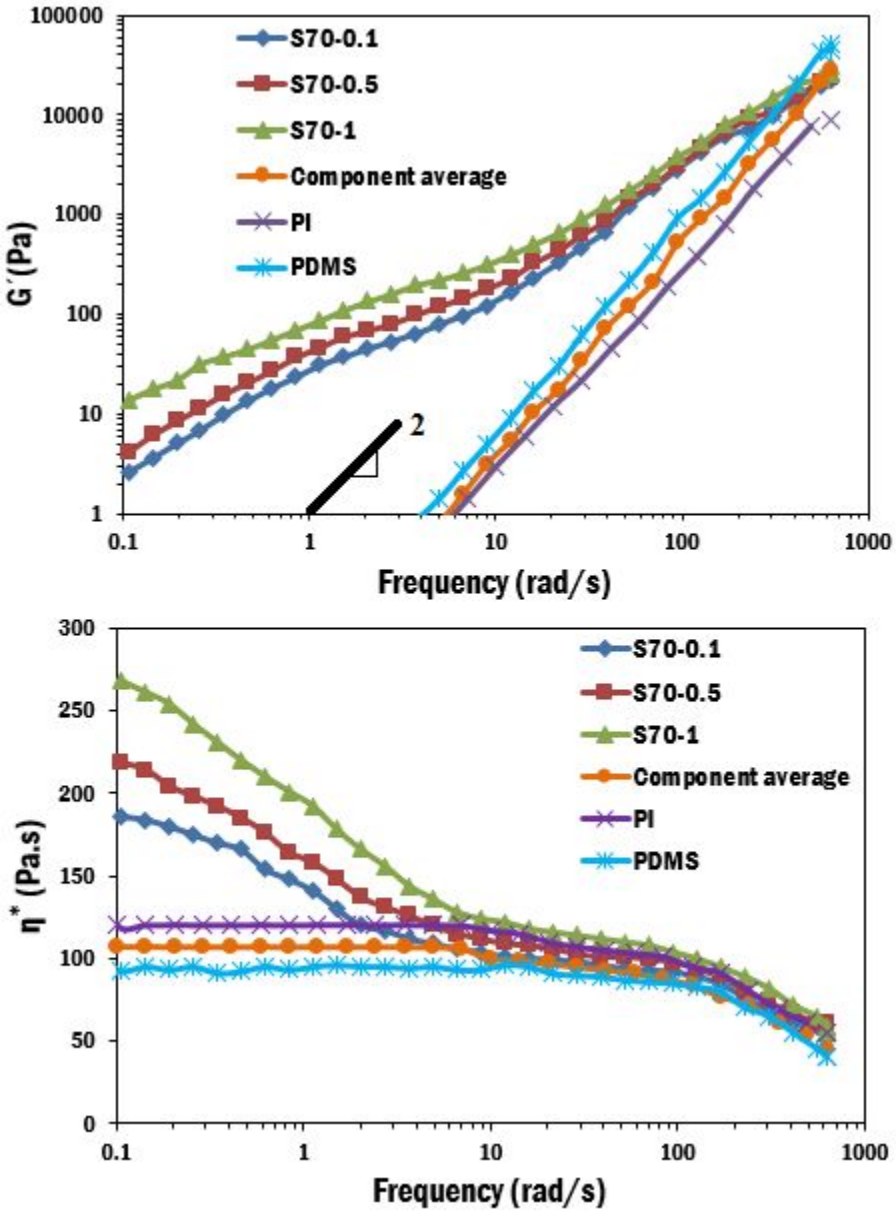

Fig. 15 As loaded oscillatory for varying ODA-GO contents in PDMS-continuous blends.

Steady shear characteristics

I. Effect of lowering stress: Coalescence suppression

Recently, Pickering emulsions containing GO or its modified substitutes were observed to be stable for several months [48-52]. The proximity of the emulsion droplets did not cause them to coalesce, which indicates that the presence of GO hinders coalescence and phase separation and thus efficiently stabilizes the emulsion. The reason the GO sheets behave this way is that the basal planes of the carbon networks and the three kinds of oxygen-containing functional groups that are on those planes endow the GO sheets with both hydrophilic and hydrophobic properties which makes them act like functional surfactants. The process of emulsification along with the GO absorption process at the interface of the two immiscible liquids leads to a reduction in the free energy of the system [49, 53]. The high surface area of the GO sheets enables them to be trapped at the interface and to wrap around the oil droplets [49, 50, 54]. Therefore, similar to Pickering emulsions stabilized with GO, the interfacial stabilization effect of ODA-GO in PI/PDMS was investigated in this section. If coalescence is effectively suppressed, a finer morphology can result because the small drops created during the most intense portion of the blending process do not recoalesce in the less intense portions. It is proposed that the ODA-GO not only makes steric hindrance in the PI/PDMS interface due to high surface area but also immobilizes their interface, greatly inhibiting the fluid in the gap from draining out and hence preventing coalescence.

As stated in the previous section, interfacial phenomena can give rise to identifiable relaxation processes in dynamic oscillatory experiments. Accordingly, the changes in drop size can be followed quantitatively by changes in the shoulder in G´. Thus, dynamic oscillatory experiments are a convenient tool to probe coalescence phenomena. These experiments followed a shear step, followed by an oscillatory step to probe changes in drop size. Directly after the initial oscillatory measurements, the blends were subjected to the shear history of Fig. 1. Figure 16a-c presents the oscillatory data recorded after shearing at 400 Pa and 50 Pa (the highest and lowest stress levels used) for S30 and S70 blends containing various amounts of GO-ODA. At 0.1% ODA-GO loading as well as in the uncompatibilized blend, the interfacial relaxation process shifted to lower frequencies upon shearing the sample at lower stresses for both

blends. The clearest indication of the shift is that G's at the two stresses now cross each other; in effect, upon shearing at low stress, G' increases at the lowest frequency, but decreases at intermediate frequencies. This slowing down of the interfacial relaxation is clearly evident in both the S30-0.1 and S70-0.1 blends and indicates growth in drop size due to coalescence. At 0.5 wt% and 1 wt% ODA-GO loadings, however, there is no significant effect of stress suggesting complete suppression of coalescence.

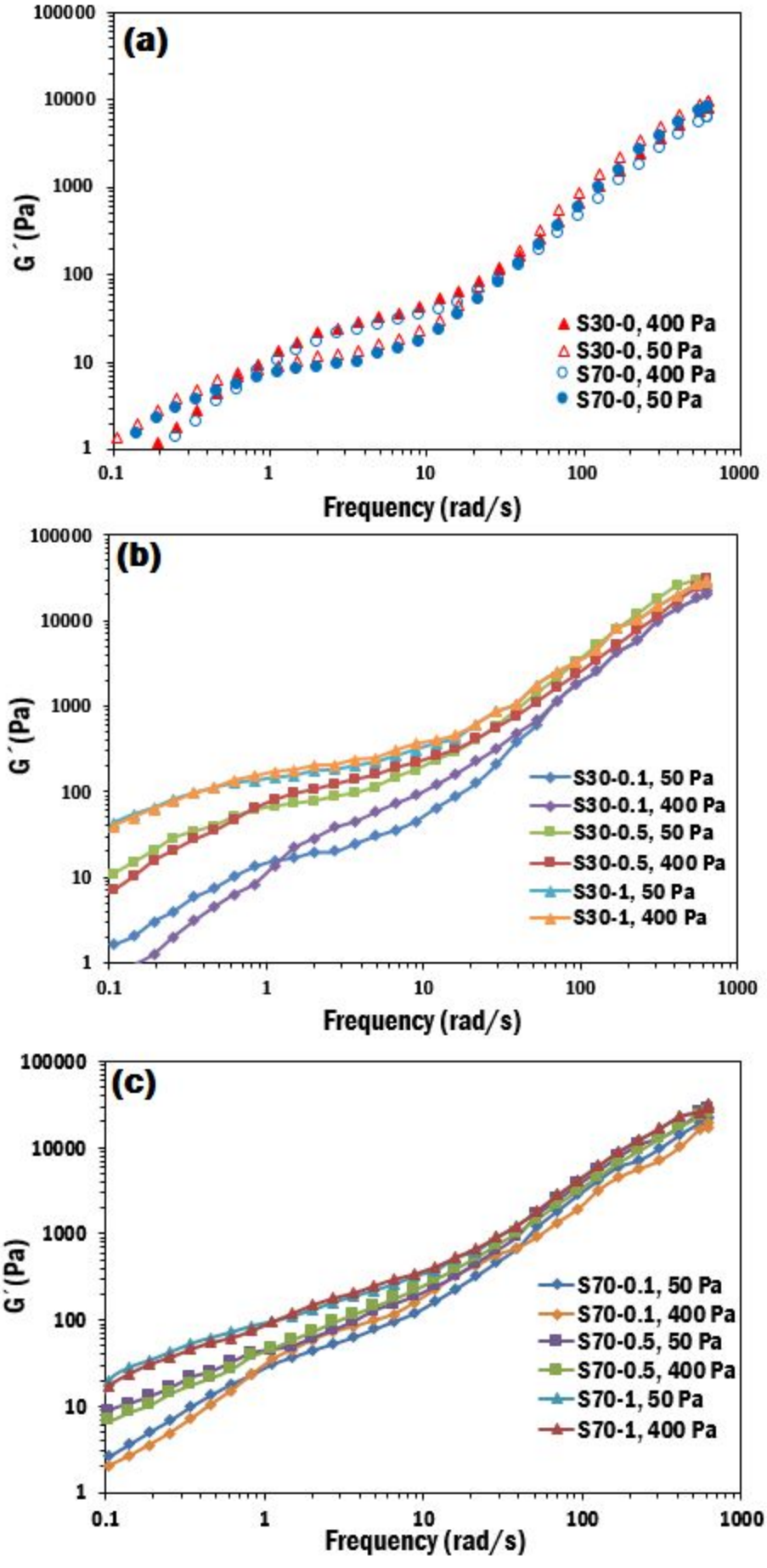
(a)
G´(Pa)
Frequency (rad/s)
S30-0, 400 Pa
S30-0, 50 Pa
S70-0, 400 Pa
S70-0, 50 Pa
(b)
G´(Pa)
Frequency (rad/s)
S30-0.1, 50 Pa
S30-0.1, 400 Pa
S30-0.5, 50 Pa
S30-0.5, 400 Pa
S30-1, 50 Pa
S30-1, 400 Pa
(c)
G´(Pa)
Frequency (rad/s)
S70-0.1, 50 Pa
S70-0.1, 400 Pa
S70-0.5, 50 Pa
S70-0.5, 400 Pa
S70-1, 50 Pa
S70-1, 400 Pa

Fig. 16 Dynamic oscillatory properties after the 400 Pa and 50 Pa shearing for blends with various ODA-GO contents (a) S30-0, S70-0, (b) S30-0.1, S30-0.5, S30-1, and (c) S70-0.1, S70-0.5, S70-1.

II. Creep behavior and steady shear viscosity

With the addition of any compatibilizer, all the steady shear viscosities of polymer blends are expected to increase as a result of the viscoelasticity of the interface [55, 56]. Therefore, to examine the processibility of the blends, we examined the creep behavior of blends at various stress levels (Fig. 17).

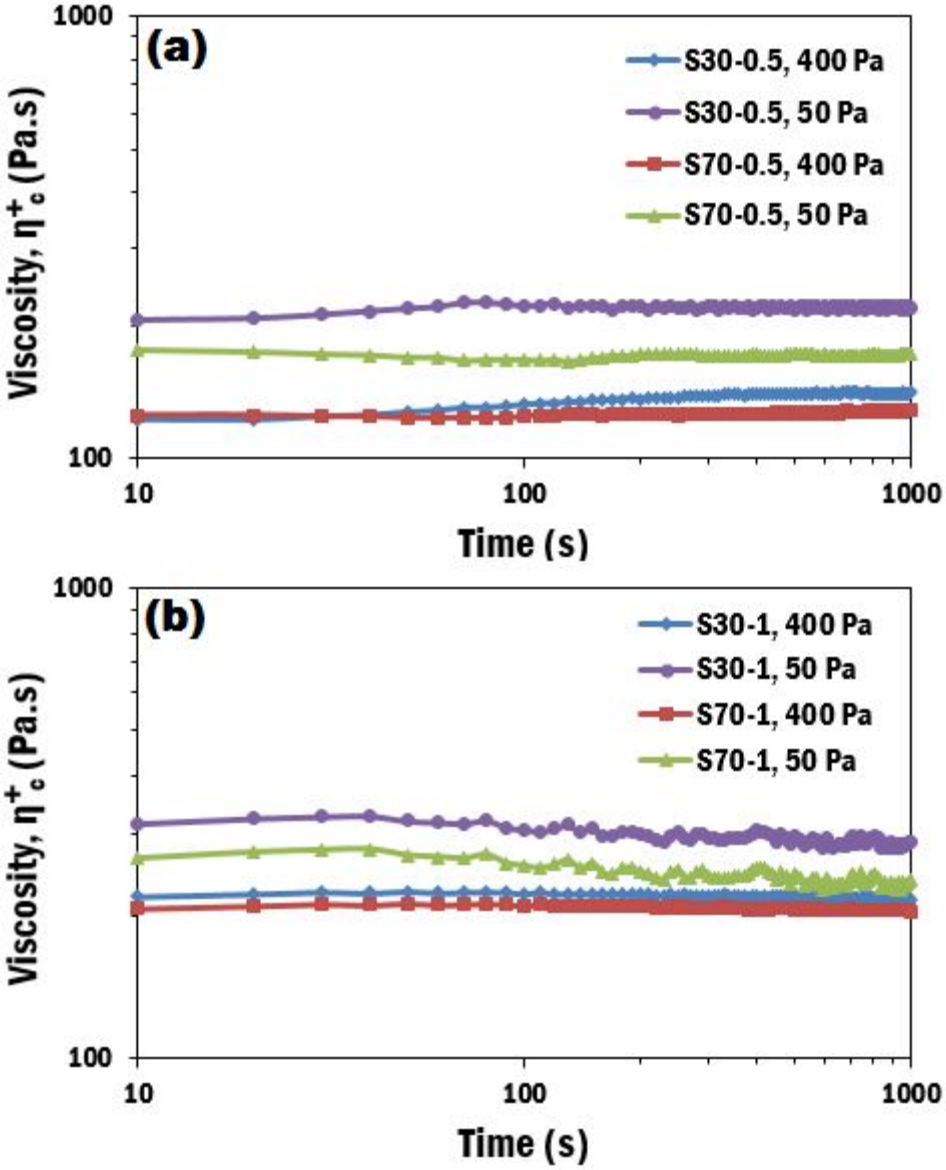

Fig. 17 Creep behavior of S30 and S70 blends with different ODA-GO content at various stress levels, (a) 0.5 wt% and (b) 1 wt%.

Figure 17 a-b shows the creep behavior of S30 and S70 blends at various stress levels with 0.5 and 1 wt% ODA-GO contents. In both samples, the lack of a viscosity overshoot is consistent with the lack of droplet aggregation which is confirmed by the OM images of Figs 10-11. On the other hand, an increase of ODA-GO contents from 0.5 to 1 wt%, raised the viscosity of both samples suggesting the strong viscoelasticity which comes from interfacially-localized ODA-GO (Fig. 12). Moreover, based on steady shear viscosity at long times at various stress levels, one can conclude that the compatibilization effect of ODA-GO results in low viscosity under steady shear indicates that they remain processible. In contrast, reactive compatibilization often causes high viscosity [57].

We now examine the relaxation time of the blends quantitatively. This analysis follows the procedure detailed previously [5, 57]. Briefly, the interfacial contribution to the storage modulus is defined as

$$G'_{interface} = G'_{measured} - G'_{component} = G'_{measured} - G'_{Palierne}\,(\alpha = 0) \quad (9)$$

where $G'_{component}$ is the bulk contribution to the modulus, obtained from the Palierne model by setting interfacial tension, α, equal to zero. $\log\left[G'_{interface}(\omega)\right]$ can then be fitted by the sum of a few Maxwell modes :

$$\log\left[G'_{interface}(\omega)\right] = \log\left[\sum_{k=1}^{n} \frac{\omega^2 \exp\,(a_k + 2t_k)}{1 + \omega^2 \exp\,(2t_k)}\right] \quad (10)$$

Here $\exp(t_k)$ and $\exp(a_k)$ are the relaxation time and the high-frequency modulus of the k^{th} Maxwell mode, respectively. The log of G' was used for fitting so that the relative error would uniformly spread across the entire frequency range. The number of modes, n, was kept at the minimum required for satisfactory fits and was never more than 3. For all compatibilized blends, $G'_{interface}$ was positive at high frequency and two or three Maxwell modes were required to obtain excellent fits. In all cases, the relaxation time of the longest Maxwell mode (the mode corresponding to the shoulder) was at least an order of magnitude higher than the other ones. This longest relaxation time is denoted as the droplet relaxation time. The obtained droplet

relaxation time is shown in Fig. 18 as a function of the shear stress. As seen previously [2, 4], the uncompatibilized S30-0 and S70-0 blends have approximately $\sigma^{-0.6}$ dependence on stress. In uncompatibilized blends, the drop size is proportional to the relaxation time and, hence, we conclude that R $\propto \sigma^{-0.6}$ in both blends. A similar dependence has been predicted by Vinckier et al. [58, 59] for a coalescence-limited morphology, albeit in a rate-controlled experiment. The Addition of 0.1% ODA-GO to S30 and S70 reduces the interfacial relaxation time by about 30% at all stresses. The stress dependence of the relaxation time of S30-0.1 and S70-0.1 remains approximately $\sigma^{-0.6}$. On the other hand, increasing the ODA-GO content to 0.5 wt% results in reduced relaxation time, suggesting small droplet sizes. In addition, for blends with 0.5 and 1 wt% GO-ODA, relaxation time is insensitive to stress, confirming indicating complete coalescence suppression at these ODA-GO loadings.

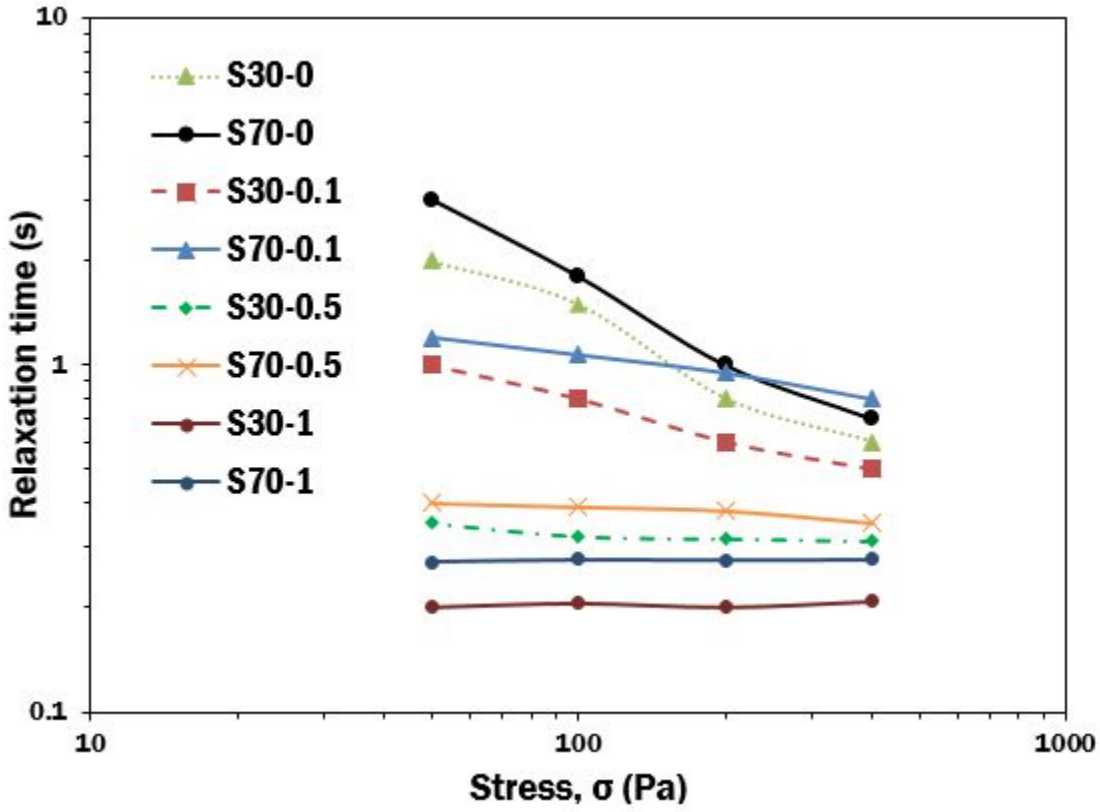

Fig. 18 Droplet relaxation time versus stress for uncompatibilized blends: S030-0, S070-0, and compatibilized blends of S030 and S070 with various ODA-GO contents.

Conclusion

In summary, we have examined the effects of interfacially localized ODA-GO content and homopolymer concentration in model blends of PI and PDMS through morphological, rheological, and electrical conductivity properties. Interfacial localization of ODA-GO between the PI/PDMS polymer phases result in stabilized droplets with fine morphology. The average droplet size decreased with ODA-GO content and both PI and PDMS-continuous blends, with no apparent droplet clustering. Increasing ODA-GO content in both blends caused deviations from liquid-like behavior in oscillatory experiments, while the steady shear viscosity remained modest, suggesting that ODA-GO does not adversely affect processability of both blends. The PI-continuous blends showed higher viscosity compared to PDMS-continuous blends. Overall we conclude that the effects of ODA-GO are two fold: by localizing at the interface, they induce interfacial viscoelasticity. Further, they completely suppress flow-induced and quiescent at sufficiently high particle loadings.

Acknowledgements

The authors are grateful to Kuraray and Rhodia for supplying the materials. We would also like to thank the center for Biological imaging at the University of Queensland for the use of their microscopy facilities and Dr. Hossein Adelnia, University of Queensland, for his advice regarding fluorescent labeling. SV is grateful to the National Science Foundation for financial support via grants 1435461 and 1561789.

References

1. Genoyer, J., N.R. Demarquette, and J. Soulestin, *Effect of clay particles size and location on coalescence in PMMA/PS blends.* Journal of Rheology, 2019. **63**(6): p. 883-893.
2. DeLeo, C., K. Walsh, and S. Velankar, *Effect of compatibilizer concentration and weight fraction on model immiscible blends with interfacial crosslinking.* Journal of Rheology, 2011. **55**(4): p. 713-731.
3. Ramachandran, R.G., et al., *Necking and drawing of rubber–plastic bilayer laminates.* Soft matter, 2018. **14**(24): p. 4977-4986.
4. DeLeo, C.L. and S.S. Velankar, *Morphology and rheology of compatibilized polymer blends: Diblock compatibilizers vs crosslinked reactive compatibilizers.* Journal of Rheology, 2008. **52**(6): p. 1385-1404.

5. Nasrollah Gavgani, J., et al., *Suppressing droplet coalescence and aggregation in immiscible homopolymer blends by interfacially cross-linked compatibilizers.* Journal of Rheology, 2018. **62**(5): p. 1217-1231.
6. Nagarkar, S.P. and S.S. Velankar, *Morphology and rheology of ternary fluid–fluid–solid systems.* Soft matter, 2012. **8**(32): p. 8464-8477.
7. Heidlebaugh, S.J., et al., *Aggregation and separation in ternary particle/oil/water systems with fully wettable particles.* Langmuir, 2014. **30**(1): p. 63-74.
8. Parpaite, T., et al., *Incorporation of modified Stöber silica nanoparticles in polystyrene/polyamide-6 blends: Coalescence inhibition and modification of the thermal degradation via controlled dispersion at the interface.* Polymer, 2014. **55**(11): p. 2704-2715.
9. Parpaite, T., et al., *Janus hybrid silica/polymer nanoparticles as effective compatibilizing agents for polystyrene/polyamide-6 melted blends.* Polymer, 2016. **90**: p. 34-44.
10. Huang, M. and H. Guo, *The intriguing ordering and compatibilizing performance of Janus nanoparticles with various shapes and different dividing surface designs in immiscible polymer blends.* Soft Matter, 2013. **9**(30): p. 7356-7368.
11. Gavgani, J.N., et al., *Intumescent flame retardant polyurethane/starch composites: thermal, mechanical, and rheological properties.* Journal of Applied Polymer Science, 2014. **131**(23).
12. Zohrevand, A., et al., *The effect of aggregation of cured rubber particles on rheology of thermoplastic vulcanizates.* Polymer Composites, 2020. **41**(4): p. 1376-1392.
13. Cavallaro, G., et al., *Modified halloysite nanotubes: nanoarchitectures for enhancing the capture of oils from vapor and liquid phases.* ACS applied materials & interfaces, 2014. **6**(1): p. 606-612.
14. Ray, S.S., et al., *Role of organically modified layered silicate as an active interfacial modifier in immiscible polystyrene/polypropylene blends.* Polymer, 2004. **45**(25): p. 8403-8413.
15. Jinhua, W., et al., *Rapid adsorption of Cr (VI) on modified halloysite nanotubes.* Desalination, 2010. **259**(1-3): p. 22-28.
16. Delbem, M.F., et al., *Modification of a Brazilian smectite clay with different quaternary ammonium salts.* Química Nova, 2010. **33**(2): p. 309-315.
17. Xi, Y., R.L. Frost, and H. He, *Modification of the surfaces of Wyoming montmorillonite by the cationic surfactants alkyl trimethyl, dialkyl dimethyl, and trialkyl methyl ammonium bromides.* Journal of colloid and interface science, 2007. **305**(1): p. 150-158.
18. Labaume, I., et al., *Comparative study of interphase viscoelastic properties in polyethylene/polyamide blends compatibilized with clay nanoparticles or with a graft copolymer.* Journal of Rheology, 2013. **57**(2): p. 377-392.
19. Tan, Y., et al., *Grafting of copolymers onto graphene by miniemulsion polymerization for conductive polymer composites: improved electrical conductivity and compatibility induced by interfacial distribution of graphene.* Polymer Chemistry, 2013. **4**(10): p. 2939-2944.
20. Fenouillot, F., P. Cassagnau, and J.-C. Majesté, *Uneven distribution of nanoparticles in immiscible fluids: Morphology development in polymer blends.* Polymer, 2009. **50**(6): p. 1333-1350.
21. Yeganeh, J.K., et al., *Controlling the kinetics of viscoelastic phase separation through self-assembly of spherical nanoparticles or block copolymers.* Soft Matter, 2014. **10**(46): p. 9270-9280.
22. Gavgani, J.N., H. Adelnia, and M.M. Gudarzi, *Intumescent flame retardant polyurethane/reduced graphene oxide composites with improved mechanical, thermal, and barrier properties.* Journal of Materials Science, 2014. **49**(1): p. 243-254.
23. Gavgani, J.N., et al., *Rheological, morphological and thermal properties of pickering-like EVA/organoclay nanocomposites.* Journal of Polymer Research, 2015. **22**(6): p. 1-17.

24. Jolfaei, A.F., et al., *Effect of organoclay and compatibilizers on microstructure, rheological and mechanical properties of dynamically vulcanized EPDM/PP elastomers.* Polymer Bulletin, 2015. **72**(5): p. 1127-1144.
25. Hong, J.S., et al., *Interfacial tension reduction in PBT/PE/clay nanocomposite.* Rheologica Acta, 2007. **46**(4): p. 469-478.
26. Elias, L., et al., *Morphology and rheology of immiscible polymer blends filled with silica nanoparticles.* Polymer, 2007. **48**(20): p. 6029-6040.
27. Ville, J., et al., *Structural and rheological investigation of interphase in polyethylene/polyamide/nanoclay ternary blends.* Polymer, 2012. **53**(8): p. 1733-1740.
28. Bai, L., et al., *Localizing graphene at the interface of cocontinuous polymer blends: Morphology, rheology, and conductivity of cocontinuous conductive polymer composites.* Journal of Rheology, 2017. **61**(4): p. 575-587.
29. Li, W., et al., *Simultaneous surface functionalization and reduction of graphene oxide with octadecylamine for electrically conductive polystyrene composites.* Carbon, 2011. **49**(14): p. 4724-4730.
30. Ma, H.-L., et al., *Functionalization and reduction of graphene oxide with p-phenylene diamine for electrically conductive and thermally stable polystyrene composites.* ACS applied materials & interfaces, 2012. **4**(4): p. 1948-1953.
31. Graziano, A., et al., *Impact of Reduced Graphene Oxide on structure and properties of polyethylene rich binary systems for performance-based applications.* Polymer, 2020. **202**: p. 122622.
32. Graziano, A., et al., *Functionally tuned nanolayered graphene as reinforcement of polyethylene nanocomposites for lightweight transportation industry.* Carbon, 2020. **169**: p. 99-110.
33. Legge, E.J., et al., *Determining the Level and Location of Functional Groups on Few-Layer Graphene and Their Effect on the Mechanical Properties of Nanocomposites.* ACS applied materials & interfaces, 2020. **12**(11): p. 13481-13493.
34. Kol, A., S. Kenig, and N. Naveh, *Silane-Modified Graphene Oxide as a Compatibilizer and Reinforcing Nanoparticle for Immiscible PP/PA Blends.* Polymer Engineering & Science, 2020. **60**(1): p. 180-191.
35. Najafi, F., et al., *Toughening of graphene-based polymer nanocomposites via tuning chemical functionalization.* Composites Science and Technology, 2020. **194**: p. 108140.
36. Fu, Y., L. Liu, and J. Zhang, *Manipulating dispersion and distribution of graphene in PLA through novel interface engineering for improved conductive properties.* ACS applied materials & interfaces, 2014. **6**(16): p. 14069-14075.
37. Graziano, A., et al., *Novel functional graphene and its thermodynamic interfacial localization in biphasic polyolefin systems for advanced lightweight applications.* Composites Science and Technology, 2020. **188**: p. 107958.
38. Gavgani, J.N., et al., *Lightweight flexible polyurethane/reduced ultralarge graphene oxide composite foams for electromagnetic interference shielding.* RSC advances, 2016. **6**(33): p. 27517-27527.
39. Huang, Y.-L., et al., *Effect of extended polymer chains on properties of transparent graphene nanosheets conductive film.* Journal of Materials Chemistry, 2011. **21**(45): p. 18236-18241.
40. Yang, D., et al., *Chemical analysis of graphene oxide films after heat and chemical treatments by X-ray photoelectron and Micro-Raman spectroscopy.* Carbon, 2009. **47**(1): p. 145-152.
41. Bourlinos, A.B., et al., *Graphite oxide: chemical reduction to graphite and surface modification with primary aliphatic amines and amino acids.* Langmuir, 2003. **19**(15): p. 6050-6055.
42. Zhou, T., et al., *A simple and efficient method to prepare graphene by reduction of graphite oxide with sodium hydrosulfite.* Nanotechnology, 2010. **22**(4): p. 045704.

43. Aboutalebi, S.H., et al., *Spontaneous formation of liquid crystals in ultralarge graphene oxide dispersions.* Advanced Functional Materials, 2011. **21**(15): p. 2978-2988.
44. Trifkovic, M., et al., *Stabilization of PE/PEO cocontinuous blends by interfacial nanoclays.* Macromolecules, 2015. **48**(13): p. 4631-4644.
45. Alexandris, S., et al., *Interfacial energy and glass temperature of polymers confined to nanoporous alumina.* Macromolecules, 2016. **49**(19): p. 7400-7414.
46. Levine, S., B.D. Bowen, and S.J. Partridge, *Stabilization of emulsions by fine particles I. Partitioning of particles between continuous phase and oil/water interface.* Colloids and surfaces, 1989. **38**(2): p. 325-343.
47. Lin, Y., et al., *Nanoparticle assembly and transport at liquid-liquid interfaces.* Science, 2003. **299**(5604): p. 226-229.
48. Hu, J., et al., *One-pot preparation of zwitterionic graphene nanosheets with exceptional redispersibility and its application in pickering emulsions.* Carbon, 2019.
49. Edgehouse, K., et al., *Stabilization of oil-in-water emulsions with graphene oxide and cobalt oxide nanosheets and preparation of armored polymer particles.* Journal of colloid and interface science, 2019. **541**: p. 269-278.
50. Luo, Q., et al., *Ionic liquid-containing pickering emulsions stabilized by graphene oxide-based surfactants.* Langmuir, 2018. **34**(34): p. 10114-10122.
51. Nagarajan, S., et al., *Porous gelatin membrane obtained from pickering emulsions stabilized by graphene oxide.* Langmuir, 2018. **34**(4): p. 1542-1549.
52. Wang, X., et al., *Self-assembling GO/modified HEC hybrid stabilized pickering emulsions and template polymerization for biomedical hydrogels.* Carbohydrate polymers, 2019. **207**: p. 694-703.
53. He, Y., et al., *Factors that affect pickering emulsions stabilized by graphene oxide.* ACS applied materials & interfaces, 2013. **5**(11): p. 4843-4855.
54. Imperiali, L., et al., *Interfacial rheology and structure of tiled graphene oxide sheets.* Langmuir, 2012. **28**(21): p. 7990-8000.
55. Velankar, S., et al., *Steady-shear rheological properties of model compatibilized blends.* Journal of Rheology (1978-present), 2004. **48**(4): p. 725-744.
56. Friedrich, C. and Y.Y. Antonov, *Interfacial relaxation in polymer blends and gibbs elasticity.* Macromolecules, 2007. **40**(4): p. 1283-1289.
57. DeLeo, C., K. Walsh, and S. Velankar, *Effect of compatibilizer concentration and weight fraction on model immiscible blends with interfacial crosslinking.* Journal of Rheology (1978-present), 2011. **55**(4): p. 713-731.
58. Vinckier, I., et al., *Droplet size evolution during coalescence in semiconcentrated model blends.* AIChE journal, 1998. **44**(4): p. 951-958.
59. Vinckier, I., P. Moldenaers, and J. Mewis, *Relationship between rheology and morphology of model blends in steady shear flow.* Journal of Rheology, 1996. **40**(4): p. 613-631.